JOURNAL OF IRON AND STEEL RESEARCH, INTERNATIONAL. 2016, 23(12):1297-1302

Deformation Behavior of Ti-5.6Al-4.8Sn-2.0Zr-1.0Mo-0.35Si-0.85Nd Alloy in β/Quasi-β Forging Process

Ke-lu WANG, Shi-qiang LU, Xian-juan DONG, Xin LI, De-lai OUYANG
(School of Aeronautical Manufacturing Engineering, Nanchang Hangkong University, Nangchang 330063, Jiangxi, China)

Abstract: The hot deformation behavior of Ti-5.6Al-4.8Sn-2.0Zr-1.0Mo-0.35Si-0.85Nd alloy in β/quasi-β forging process was studied using isothermal compression tests over temperature range from 1040 ℃ to 1100 ℃ and strain rates form 0.001 s^{-1} to 70 s^{-1}. The results show that the flow stress and microstructure are sensitive to thermomechanical parameters. The processing maps based on the dynamic materials model at strain of 0.3 and 0.7 were established. The optimum deformation thermomechanical parameters at a strain of 0.7 have two regions that exhibit the peak of power dissipation efficiency. One is the region of 1062—1100 ℃ and 10^{-3}—$10^{-1.5}$ s^{-1}; and another which represents dynamic recrystallization is 1040—1045 ℃ and $10^{-1.8}$—$10^{-0.9}$ s^{-1}. The instable region is located where the strain rate is larger than 1 s^{-1} which corresponds to the mechanical instability.

Key words: titanium alloy; β/quasi-β forging; deformation behavior; processing map; process parameters optimization

Titanium alloy has already been extensively used in aeronautic, shipbuilding, biomedical, pharmaceutical and chemical industry due to their excellent properties including high specific strength, low density and good corrosion resistance[1]. As a new titanium alloy, Ti-5.6Al-4.8Sn-2.0Zr-1.0Mo-0.35Si-0.85Nd alloy has been used in fabrication of the aerofoil blades and discs in the aircraft industry owing to its good creep resistance and thermo-stability at the servicing temperatures of 600 ℃[2,3]. The alloy is generally formed in the temperature range of 30—50 ℃ below β transus (namely α+β forging). In α+β forging, the microstructure of titanium alloy obtained is equiaxed, and it has high plasticity and thermal stability. However, its high temperature properties, fatigue capability, and fracture toughness under the service temperature are unsatisfactory[4,5].

Compared with α+β forging alloys, the β forging has basket weave structure and shows better high temperature creep resistance and fracture toughness; but its plasticity and thermal stability is obviously reduced, resulting in 'β brittleness' and 'microstructural inheritance'[6,7]. Recently, Zhu et al.[8] prepared a quasi-β forging technology with the temperature range of (T_β—10)—(T_β+20) ℃ (T_β is the β-transus temperature). This process was applicable to near α, α+β and near β titanium alloys, and lamellar α phase content obtained in this process was not more than 15%; the fracture toughness, fatigue crack propagation resistance and creep resistance were significantly higher than those of the duplex microstructure.

The determination and optimization of process parameters are still lack of systematic and theoretical guidance for the β/quasi-β forging process of titanium alloys. In this work, the flow stress of Ti-5.6Al-4.8Sn-2.0Zr-1.0Mo-0.35Si-0.85Nd alloy was obtained by hot compression test, and the effects of deformation thermomechanical parameters on the true stress were analyzed. The processing maps of the alloy were established, and the optimum thermal deformation parameters were obtained, which can provide the theoretical foundation for the microstructure control and process optimization in β/qua-

Foundation Item: Item Sponsored by National Natural Science Foundation of China (51164030, 51261020); Education Commission Foundation of Jiangxi Province of China (GJJ13501)

Biography: Ke-lu WANG, Doctor, Professor; **E-mail**: wangkelu@126.com; **Received Date**: December 19, 2015

si-β forging processes of titanium alloys.

1 Material and Experimental Procedures

The β-transus temperature of the tested alloy is 1040 ℃. The initial microstructure is lath-shaped microstructure, as shown in Fig. 1.

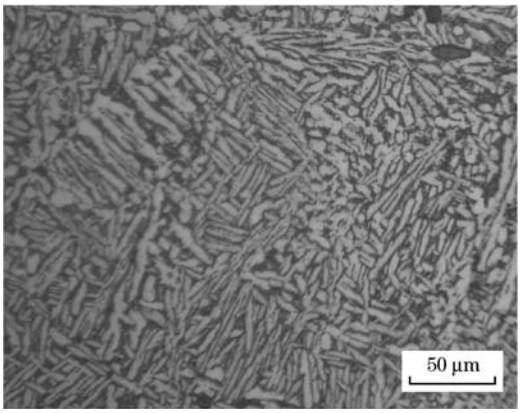

Fig. 1 Billet microstructure of the tested alloy

The compression experiments were performed by using a Thermecmaster-Z simulator under constant strain rate and temperature each time. The sample was a cylinder with the dimension of ϕ8 mm×12 mm, and a groove with the depth of 0.2 mm was made on the two ends for holding lubricant. The specimens were heated at a rate of 10 ℃/s until the required temperature was reached, and the holding time was 300 s. The compression tests were performed at temperatures of 1040 — 1100 ℃, strain rates of 0.001 — 70 s^{-1} to a height reduction of 50%, and the corresponding effective strain was about 0.7. The specimens were then cooled to room temperature by spraying helium after deformation.

2 Results and Discussion

2.1 True stress-strain curves

Fig. 2 shows the true stress-strain curves at different temperatures and strain rates. The flow stress increased with the rise of strain rate, while decreased

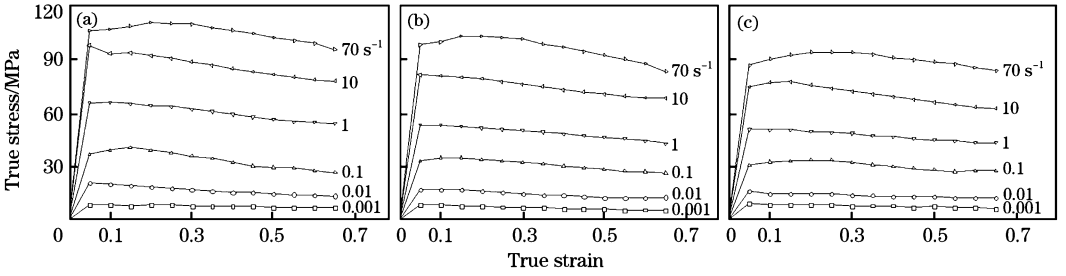

Fig. 2 Stress-strain curves at 1040 ℃ (a), 1070 ℃ (b) and 1100 ℃ (c)

with the increase of temperature. The true stress-strain curves of the alloy under different thermomechanical parameters showed that the true stress reached the maximum value quickly at the early stage of compression because of working hardening. From Fig. 2, if the strain rate is larger than 1 s^{-1}, the true stress has a peak value when the strain reaches a critical value, and then decreases with the increase of strain. Obviously, there is a flow softening behavior. While the strain rate is slower than 1 s^{-1}, the curves become smooth and appear to have a steady-state characteristic with the increase of strain.

2.2 Kinetic analysis of deformation behavior

The combined effects of deformation temperature and strain rate on the stress are usually described by the kinetic rate equation as follows[9,10]:

$$\dot{\varepsilon}\exp\left(\frac{Q}{RT}\right)=A_1\exp(n_1\sigma) \tag{1}$$

$$\dot{\varepsilon}\exp\left(\frac{Q}{RT}\right)=A_2\sigma^{n_2} \tag{2}$$

$$\dot{\varepsilon}\exp\left(\frac{Q}{RT}\right)=A_3\sinh(\alpha\sigma)^{n_3} \tag{3}$$

where, $\dot{\varepsilon}$ is the strain rate, s^{-1}; σ is the true stress, MPa; Q is the activation energy of deformation, kJ·mol^{-1}; R is the gas constant, 8.314 kJ·mol^{-1}·K^{-1}; and T is the deformation temperature, K. Moreover, A_1, A_2, A_3, n_1, n_2, n_3 and α ($=n_1/n_2$) are the materials parameters.

Natural logarithm is taken at both sides of Eqs. (1), (2) and (3), and the following equations can be obtained:

$$\sigma=\frac{1}{n_1}\ln\dot{\varepsilon}+\frac{Q}{n_1RT}-\frac{\ln A_1}{n_1} \tag{4}$$

$$\ln\sigma=\frac{1}{n_2}\ln\dot{\varepsilon}+\frac{Q}{n_2RT}-\frac{\ln A_2}{n_2} \tag{5}$$

$$\ln[\sinh(\alpha\sigma)]=\frac{1}{n_3}\ln\dot{\varepsilon}+\frac{Q}{n_3RT}-\frac{\ln A_3}{n_3} \tag{6}$$

Then, substitute the values of stress and corresponding strain rates under the strain of 0.4 into Eqs. (4) and (5). And then, Eqs. (4) and (5) are plot-

ted in the form of $\ln\dot{\varepsilon}$-σ and $\ln\dot{\varepsilon}$-$\ln\sigma$, respectively. This is shown in Figs. 3(a) and 3(b). At each temperature, the values of n_1 and n_2 depend on slopes in the two plots. Because of the values of n_1 and n_2 are different according to different temperatures, their average values are applied to be calculated. And then the parameter α can be calculated, whose value is about 0.028363 MPa^{-1}.

The activation energy for the plastic flow, Q in Eq. (3) is calculated using Eq. (7)[11]:

$$Q = R\left[\frac{\partial \ln\dot{\varepsilon}}{\partial \ln[\sinh(\alpha\sigma)]}\right]_T \left[\frac{\partial \ln[\sinh(\alpha\sigma)]}{\partial(1/T)}\right]_{\dot{\varepsilon}} = n_3 Rk \tag{7}$$

where, $n_3 = \left[\frac{\partial \ln\dot{\varepsilon}}{\partial \ln[\sinh(\alpha\sigma)]}\right]_T$ is the stress constant measured form the curves of $\ln\dot{\varepsilon}$-$\ln[\sinh(\alpha\sigma)]$ at a given temperature; and $k = \left[\frac{\partial \ln[\sinh(\alpha\sigma)]}{\partial(1/T)}\right]_{\dot{\varepsilon}}$ is the slope measure in the plot of $\ln[\sinh(\alpha\sigma)]$-10 000/T at a given strain rate, as shown in Fig. 4.

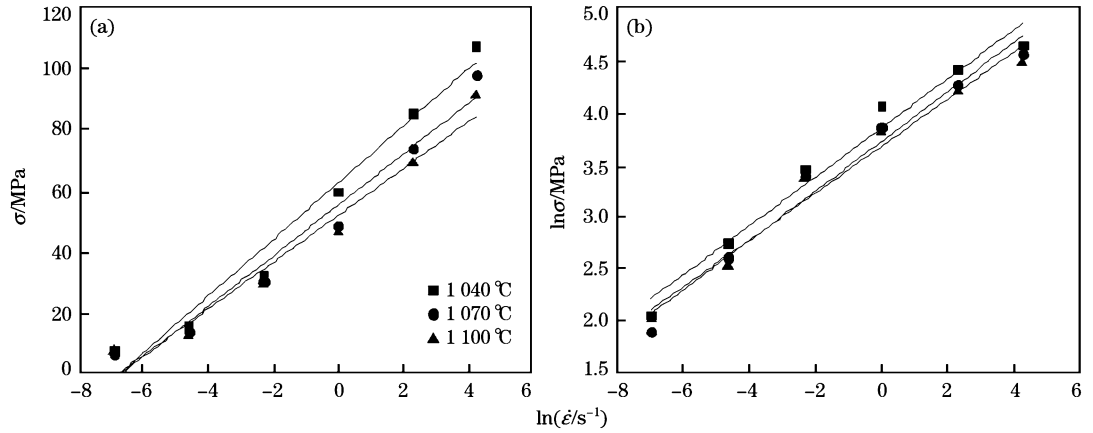

Fig. 3 Plots of $\ln\dot{\varepsilon}$-σ (a) and $\ln\dot{\varepsilon}$-$\ln\sigma$ (b) for tested alloy

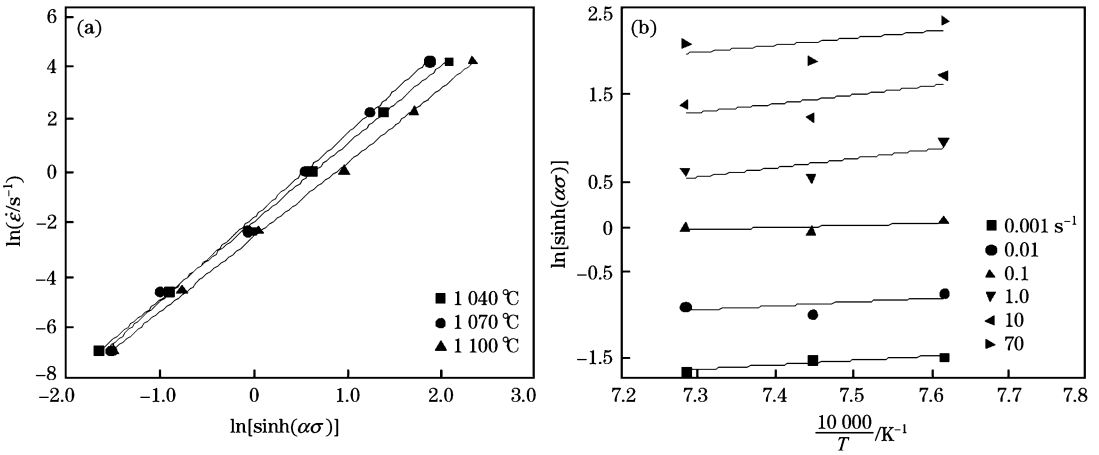

Fig. 4 Plots of $\ln\dot{\varepsilon}$-$\ln[\sinh(\alpha\sigma)]$ (a) and $\ln[\sinh(\alpha\sigma)]$-(10 000/T) (b) for the tested alloy

As a result, the values of n_3 and k are determined by the average slope of two groups of lines. The activation energy of the tested alloy obtained in β/quasi-β forging process is about 493.8 kJ/mol, which is larger than that of self-diffusion (153 kJ/mol). It shows that these deformation behaviors are not mainly determined by the diffusion mechanism. The dynamic recrystallization may play a prominent part in β/quasi-β forging process of the titanium alloy.

2.3 Processing maps

2.3.1 Theory of processing map

The processing map is established on the basis of dynamic materials model (DDM). The total power P is dissipated in two ways: the viscoplastic heat (represented by G) and internal microstructural evolution including dynamic recovery, dynamic recrystallization, etc. in deformation process (represented by J). The relationship between G and J is expressed as[12]:

$$P=\sigma\dot{\varepsilon}=G+J=\int_0^{\dot{\varepsilon}}\sigma\,\mathrm{d}\dot{\varepsilon}+\int_0^{\sigma}\dot{\varepsilon}\,\mathrm{d}\sigma \quad (8)$$

When temperature and strain are kept constant, the stress can be expressed using the following formula[13]:

$$\sigma=K\dot{\varepsilon}^{m} \quad (9)$$

where, K is a constant; and m is the strain rate sensitivity, which is defined by following formula:

$$m=\partial\ln\sigma/\partial\ln\dot{\varepsilon} \quad (10)$$

The power dissipation capacity of the materials given by a dimensionless parameter is referred to the power dissipation efficiency η. It can be described as Eq. (11)[14]:

$$\eta=2m/(m+1) \quad (11)$$

As η is determined by strain, strain rate and temperature, when strain is a constant, it will depend on strain rate and temperature. The dependence of η on temperature and strain rate can be expressed by the power dissipation map.

The instability criterion for flow instability is defined according to another parameter[15]:

$$\xi(\dot{\varepsilon})=\frac{\partial\ln(m/m+1)}{\partial\ln\dot{\varepsilon}}+m<0 \quad (12)$$

As $\xi(\dot{\varepsilon})$ is the instability factor, when $\xi(\dot{\varepsilon})$ is negative to a certain deformation condition, the metallurgical instability occurs. The instability map can be obtained by plotting $\xi(\dot{\varepsilon})$ at different temperatures and different strain rates where $\xi(\dot{\varepsilon})$ is negative.

2.3.2 Power dissipation efficiency

The power dissipation efficiency of the tested alloy is shown in Fig. 5. It can be easily observed that the strain rate has significant impact on the η value. The η value of tested alloy decreases with the increase of strain rate at a given temperature and strain of 0.3. When the strain is 0.7, the curve of η value at temperature of 1070 and 1100 ℃ is similar to that of strain of 0.3. At 1040 ℃, the η increased to the maximum with the increase of strain rate at the beginning after it decreased to a lower value.

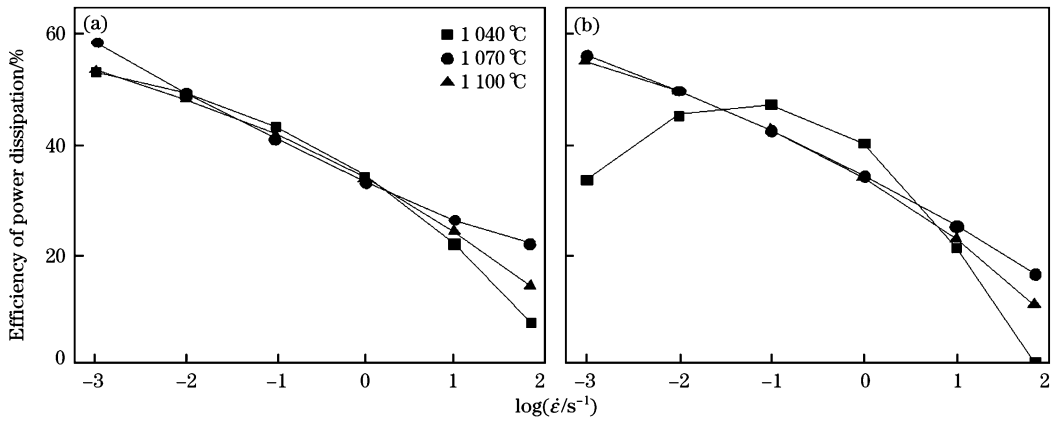

Fig. 5 Changing laws of η at strains of 0.3 (a) and 0.7 (b)

2.3.3 Flow instability factor

Fig. 6 shows the relationship between the value of instability factor and the strain rate when the strain and temperature are constant. From Fig. 6, it can be found that the strain rate also has noticeable impact on the instability factor. Its influence is similar to that of power dissipation efficiency.

2.3.4 Processing maps

According to Eqs. (11) and (12), the processing maps of the tested alloy in the temperature range of 1040—1100 ℃ and strain rate of 0.001—70 s^{-1} at the strains of 0.3 and 0.7 are developed in Fig. 8, indicating the stable region and instable region during plastic processing. The contour numbers represent the η value and the shaded regions are the instability regions. As observed from Fig. 7(a), the processing map has a region that exhibits the peak value of η at strain rate of 10^{-3} — 10^{-2} s^{-1} and temperature of 1050—1100 ℃ with a peak value about 59% at 1080 ℃/10^{-3} s^{-1} and a true strain of 0.3. The processing map for the present alloy obtained at a strain of 0.7 is shown in Fig. 7(b), which exhibits two peak regions given as follows: (1) 1062—1100 ℃ and 10^{-3}—$10^{-1.5}$ s^{-1} and the peak efficiency is about 60% occurring at 1080 ℃ and 10^{-3} s^{-1}; and (2) 1040—1045 ℃ and $10^{-1.8}$—$10^{-0.9}$ s^{-1} with a peak efficiency of 53% occurring at 1040 ℃ and $10^{-1.4}$ s^{-1}. According to Prasad[16] and Murty et al.[17], the workability is better in stable region. In the processing map, an instable region occurs when the strain rate rises above approximately 1 s^{-1} under the tested process parameters, which is shown in Fig. 7. With increasing strain, the flow instability region becomes bigger. Thus, the corresponding thermomechanical par-

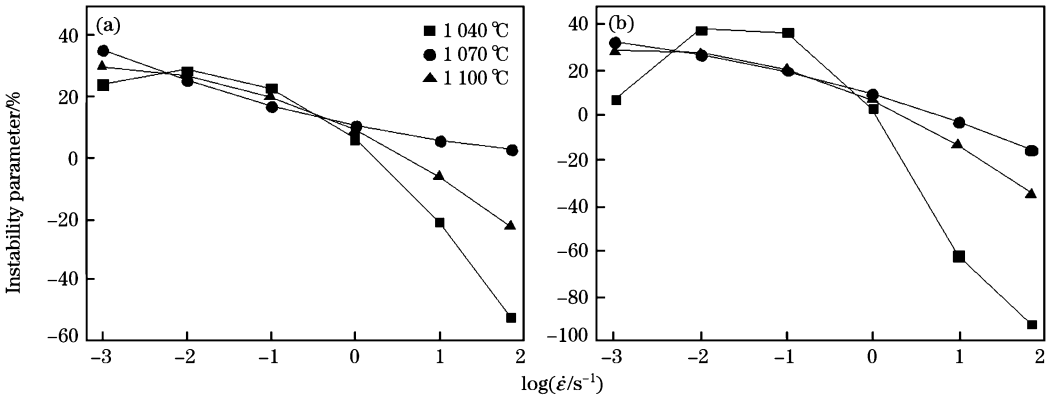

Fig. 6 Changing laws of $\xi(\dot{\varepsilon})$ at strains of 0.3 (a) and 0.7 (b)

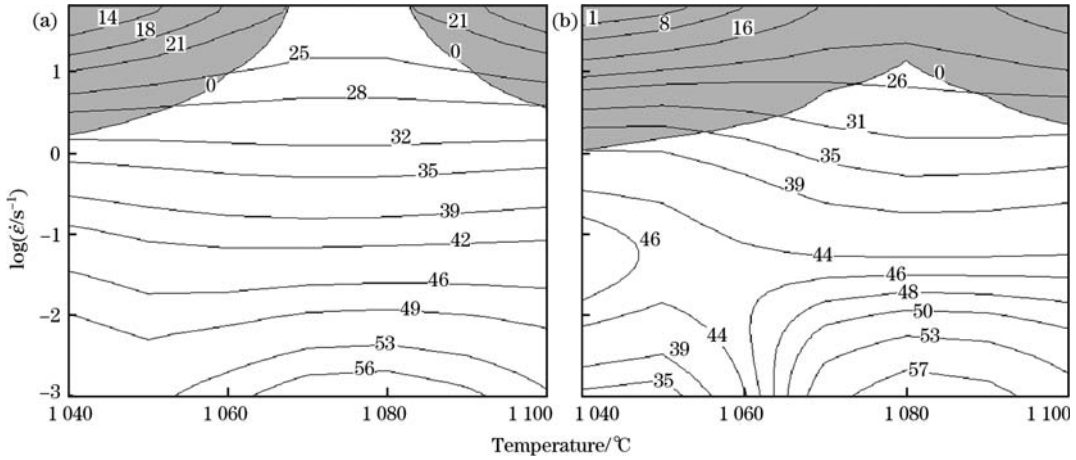

Fig. 7 Processing maps of the tested alloy at strains of 0.3 (a) and 0.7 (b)

ameters of this region cannot be selected in the practical application demands. Therefore, the optimum processing regions may occur at lower strain rate. However, some power dissipation mechanism with large η value is also damage type in processing maps. It is used in analysis of microstructural characteristics after deformation, combined with processing map, to determine the deformation mechanisms.

2.3.5 Deformation microstructure

Figs. 8 and 9 show the microstructures of the present alloy deformed at different temperatures and strain rates. When deformed at high strain rate (Figs. 8 (a) and 8(b) in instable region), which corresponds to the mechanical instability formation, the β grains are

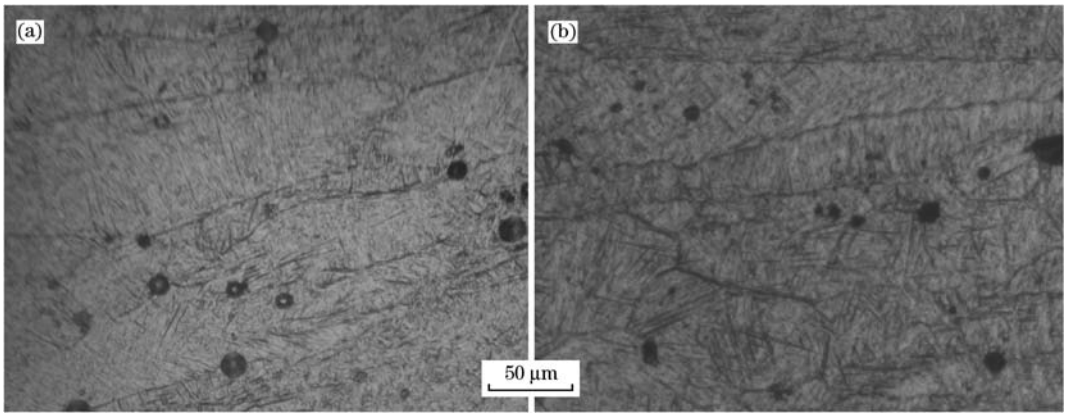

Fig. 8 Optical microstructures of present alloy deformed at 1 040 ℃/70 s^{-1} (a) and 1 100 ℃/10 s^{-1} (b) exhibiting mechanical instability in the instability regions respectively in processing map (true strain of 0.7)

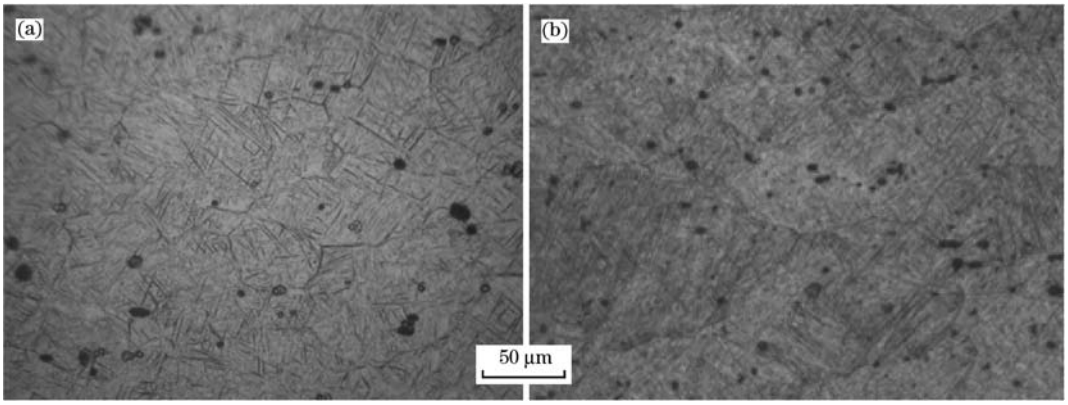

Fig. 9 Optical microstructures of present alloy deformed at 1040 ℃/0.1 s^{-1} (a) and 1100 ℃/0.001 s^{-1} (b) exhibiting dynamic recrystallization and grain coarsening in the peak regions of η respectively in processing map (true strain of 0.7)

elongated in the direction of the main deformation, and there are some fine dynamic recrystallization grains on the original coarse grain boundary. The deformation microstructure heterogeneity will result in nonuniformity of mechanical properties.

Sound deformation thermomechanical parameters can be obtained when deformed at low strain rate, such as 1040 ℃/0.1 s^{-1} and 1070 ℃/0.001 s^{-1} (Figs. 9(a) and 9(b) in stable region). According to the microstructure observed, in the processing maps, regions that have high η value occurs at 1062—1100 ℃ and 10^{-3}—$10^{-1.5}$ s^{-1} or at 1040—1045 ℃ and $10^{-1.8}$—$10^{-0.9}$ s^{-1}. It can be identified as dynamic recrystallization and grain coarsening after dynamic recrystallization.

In summary, the optimum deformation thermomechanical parameters at a strain of 0.7 is as follows: (1) at the strain rate range of around 10^{-3}—$10^{-1.5}$ s^{-1} and temperature range between 1062 and 1100 ℃, with η value of around 46%—60%; and (2) 1040—1045 ℃ and $10^{-1.8}$—$10^{-0.9}$ s^{-1} with η value of around 44%—53%.

3 Conclusions

(1) The processing maps were established respectively based on the DMM. The optimum deformation thermomechanical parameters at a strain of 0.7 have two regions that exhibit the peak of power dissipation efficiency as follows: one is 1062—1100 ℃ and 10^{-3}—$10^{-1.5}$ s^{-1}; and another is 1040—1045 ℃ and $10^{-1.8}$—$10^{-0.9}$ s^{-1}. The main plastic deformation mechanism is identified as dynamic recrystallization.

(2) The instable region is located under where the strain rate is larger than 1 s^{-1} which corresponds to the mechanical instability.

References:

[1] C. Deng, Y. Wang, Y. P. Zhang, J. C. Gao, J. Iron Steel Res. Int. 14 (2007) No. 3, 73-78.
[2] L. N. Yang, J. R. Liu, J. Tan, Z. Y. Chen, Q. J. Wang, R. Yang, J. Mater. Sci. Technol. 30 (2014) 706-709.
[3] Z. L. Zhao, H. Li, M. W. Fu, H. Z. Guo, Z. K. Yao, J. Alloys Comp. 617 (2014) 525-533.
[4] I. Balasundar, T. Raghu, B. P. Kashyap, Mater. Sci. Eng. A 609 (2014) 241-249.
[5] H. M. Flower, Mater. Sci. Technol. 6 (1990) 1082-1092.
[6] K. L. Wang, S. Q. Lu, M. W. Fu, X. Li, X. J. Dong, Mater. Charact. 60 (2009) 492-498.
[7] Z. C. Sun, F. X. Han, H. L. Wu, H. Yang, J. Mater. Process. Technol. 229 (2016) 72-81.
[8] Z. S. Zhu, Q. R. Wang, Y. L. Zheng, Quasi-β Forging Technology of Titanium Alloy, China, CN1403622, 2001.
[9] M. Sarebanzadeh, R. Mahmudi, R. Roumina, Mater. Sci. Eng. A 637 (2015) 155-161.
[10] E. X. Pu, W. J. Zheng, Z. G. Song, J. Z. Xiang, X. P. Wei, J. Iron Steel Res. Int. 21 (2014) 975-982.
[11] B. Wu, M. Q. Li, D. W. Ma, Mater. Sci. Eng. A 542 (2012) 79-87.
[12] Y. V. R. K. Prasad, H. L. Gegel, Metall. Mater. Trans. A 15 (1984) 1883-1892.
[13] L. Wang, G. Yang, T. Lei, S. B. Yin, L. Wang, J. Iron Steel Res. Int. 22 (2015) 1043-1048.
[14] S. B. Bhimavarapu, A. K. Maheshwari, D. Bhargava, S. P. Narayan, J. Mater. Sci. 46 (2011) 3191-3199.
[15] A. Łukaszek-Sołek, J. Krawczyk, Mater. Des. 65 (2015) 165-173.
[16] Y. V. R. K. Prasad, Metall. Trans. A 27 (1996) 235-247.
[17] S. V. S. N. Murty, B. N. Rao, B. P. Kashyap, Int. Mater. Rev. 45 (2000) 15-26.